

# Fluid-enhanced surface diffusion controls intraparticle phase transformations

Yiyang Li<sup>1,2,13</sup>, Hungru Chen<sup>3</sup>, Kipil Lim<sup>1,4</sup>, Haitao D. Deng<sup>1</sup>, Jongwoo Lim<sup>1,2</sup>, Dimitrios Fraggdakis<sup>5</sup>, Peter M. Attia<sup>1</sup>, Sang Chul Lee<sup>1</sup>, Norman Jin<sup>1</sup>, Jože Moškon<sup>6</sup>, Zixuan Guan<sup>7</sup>, William E. Gent<sup>8</sup>, Jihyun Hong<sup>1,4</sup>, Young-Sang Yu<sup>9</sup>, Miran Gaberšček<sup>6,10</sup>, M. Saiful Islam<sup>3\*</sup>, Martin Z. Bazant<sup>1,5,11,12\*</sup> and William C. Chueh<sup>1,2\*</sup>

**Phase transformations driven by compositional change require mass flux across a phase boundary. In some anisotropic solids, however, the phase boundary moves along a non-conductive crystallographic direction. One such material is  $\text{Li}_x\text{FePO}_4$ , an electrode for lithium-ion batteries. With poor bulk ionic transport along the direction of phase separation, it is unclear how lithium migrates during phase transformations. Here, we show that lithium migrates along the solid/liquid interface without leaving the particle, whereby charge carriers do not cross the double layer. X-ray diffraction and microscopy experiments as well as ab initio molecular dynamics simulations show that organic solvent and water molecules promote this surface ion diffusion, effectively rendering  $\text{Li}_x\text{FePO}_4$  a three-dimensional lithium-ion conductor. Phase-field simulations capture the effects of surface diffusion on phase transformation. Lowering surface diffusivity is crucial towards suppressing phase separation. This work establishes fluid-enhanced surface diffusion as a key dial for tuning phase transformation in anisotropic solids.**

Solid-state phase transformations triggered by the migration of atoms and ions enable many important technologies, including batteries<sup>1</sup>, hydrogen storage<sup>2</sup>, electrocatalysts<sup>3</sup> and memristors<sup>4</sup>. In anisotropic materials, the mass flux required for phase transformations may lie along a non-conductive crystallographic direction. Because bulk mass transport is slow, phase transformations in these materials require alternative mass transport mechanisms, which are not well understood.

$\text{Li}_x\text{FePO}_4$  ( $0 < x < 1$ ) is a model phase-transforming anisotropic material<sup>5–8</sup> with a large miscibility gap for particles larger than ~50 nm (ref. <sup>9</sup>) and exhibits one-dimensional lithium migration<sup>10,11</sup>. At low (de)lithiation rates,  $\text{Li}_x\text{FePO}_4$  intercalates via a particle-by-particle pathway, first explained by the domino cascade model<sup>12</sup> and more recently by its non-monotonic Li chemical potential profile<sup>13</sup> (that is, mosaic instability<sup>14</sup>). At elevated (de)lithiation rates, density functional theory<sup>15</sup> and reaction-limited phase-field modelling<sup>16</sup> suggest that phase separation is suppressed and replaced with a solid solution pathway. This metastable solid solution was observed using operando diffraction and microscopy<sup>17–21</sup>, and the solid solution phase separates into Li-rich and Li-poor phases under equilibrium at room temperature<sup>15</sup> (Fig. 1a). Owing to anisotropic strain, the stable phase boundaries are perpendicular to the [100] and [001] directions<sup>14,21–23</sup>, indicating that lithium traverses along these directions during phase separation. Yet lithium-ion diffusion is fast in the [010] direction and essentially non-existent in the other directions<sup>10,11,24</sup>. These two central features of  $\text{Li}_x\text{FePO}_4$  present an important but unresolved question: if the bulk crystal structure does not transport lithium in the [100] and [001] directions, then how does lithium migrate during phase transformations?

There are several possible avenues for lithium transport along nominally non-conductive directions (Fig. 1b). Anti-site defects enable ion hopping between the fast conduction channels<sup>25–28</sup>, but this bulk resistance  $R_{\text{bulk}}$  is very large for particles with low anti-site defect concentrations<sup>11,25</sup>. Surfaces may enable higher transport rates, but density functional theory calculations show that the lithium surface diffusion resistance  $R_{\text{surfD}}$  at the  $\text{FePO}_4$ /vacuum interface is even higher than  $R_{\text{bulk}}$  (ref. <sup>29</sup>). Since in-plane bulk and surface diffusion are believed to be slow, the prevailing model is that lithium de-intercalates from the particle, migrates in the liquid electrolyte and re-intercalates<sup>16,18,19,30</sup>. Here, the interfacial reaction resistance  $R_{\text{rxn}}$  is assumed to be rate-limiting because of fast lithium ion transport in the electrolyte<sup>31</sup>. Many-particle phase-field simulations show that this pathway cannot result in intraparticle phase separation because the electrode prefers to phase separate between particles<sup>32,33</sup>. Such simulations, however, contradict in situ observations of intraparticle phase separation within individual particles<sup>20</sup>, and highlight an insufficient understanding of the lithium migration pathway and the phase separation mechanisms in  $\text{Li}_x\text{FePO}_4$ .

## Phase transformation in ionically isolated particles

To elucidate the phase transformation mechanisms, we first measured the rate of phase separation in ionically isolated, solid solution  $\text{Li}_{0.5}\text{FePO}_4$  microplatelet particles<sup>21,23</sup> (Supplementary Figs. 1–3). Both carbon-coated and uncoated particles were studied. These particles are ~3  $\mu\text{m}$  in the major axis, which is nearly parallel to [001], ~1.5  $\mu\text{m}$  in the minor axis, nearly parallel to [100], and ~170 nm thick in the [010] thickness direction (Supplementary

<sup>1</sup>Department of Materials Science & Engineering, Stanford University, Stanford, CA, USA. <sup>2</sup>Stanford Institute for Materials and Energy Sciences, SLAC National Accelerator Laboratory, Menlo Park, CA, USA. <sup>3</sup>Department of Chemistry, University of Bath, Bath, UK. <sup>4</sup>Stanford Synchrotron Radiation Lightsource, SLAC National Accelerator Laboratory, Menlo Park, CA, USA. <sup>5</sup>Department of Chemical Engineering, Massachusetts Institute of Technology, Cambridge, MA, USA. <sup>6</sup>National Institute of Chemistry, Ljubljana, Slovenia. <sup>7</sup>Department of Applied Physics, Stanford University, Stanford, CA, USA. <sup>8</sup>Department of Chemistry, Stanford University, Stanford, CA, USA. <sup>9</sup>Advanced Light Source, Lawrence Berkeley National Laboratory, Berkeley, CA, USA. <sup>10</sup>Faculty of Chemistry and Chemical Technology, University of Ljubljana, Ljubljana, Slovenia. <sup>11</sup>Department of Mathematics, Massachusetts Institute of Technology, Cambridge, MA, USA. <sup>12</sup>SUNCAT Interfacial Science and Catalysis, Stanford University, Stanford, CA, USA. <sup>13</sup>Present address: Sandia National Laboratories, Livermore, CA, USA. \*e-mail: [m.s.islam@bath.ac.uk](mailto:m.s.islam@bath.ac.uk); [bazant@mit.edu](mailto:bazant@mit.edu); [wchueh@stanford.edu](mailto:wchueh@stanford.edu)

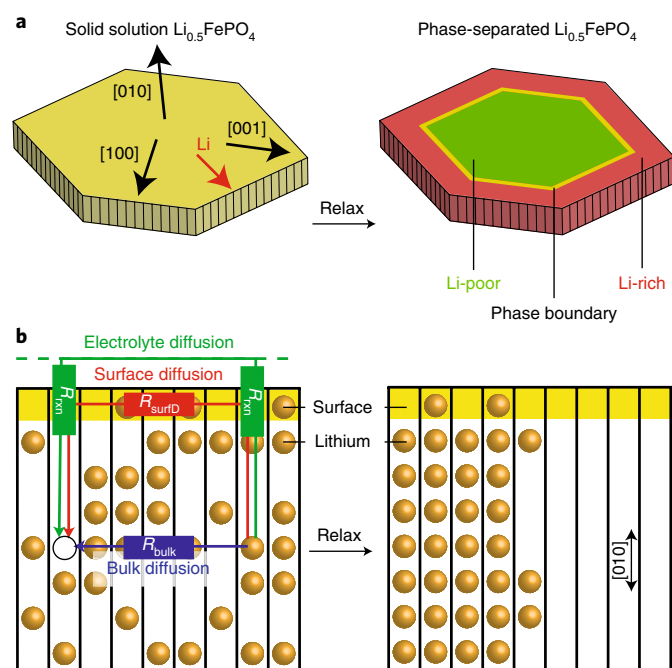


**Fig. 1 | Crystallographic directions, phase separation and in-plane lithium migration in a  $\text{Li}_{0.5}\text{FePO}_4$  platelet particle.** **a**, Solid solution  $\text{Li}_x\text{FePO}_4$  separates into Li-rich and Li-poor phases. The phase boundaries lie along the  $ab$  and  $bc$  planes, and perpendicular to the  $[100]$  and  $[001]$  directions. Therefore, lithium must migrate in the  $[100]$  and  $[001]$  directions. The  $[001]$  direction is the major axis along the plane, whereas the  $[100]$  direction is the minor axis. **b**, Cross-section schematic view of the crystallographic directions. Three possible in-plane migration paths are possible: bulk diffusion, surface diffusion and electrolyte diffusion in conjunction with interfacial (de)lithiation reactions. The dashed green lines indicate that electrolyte diffusion enables lithium transport between particles. The relative resistances of these three paths ( $R_{\text{bulk}}$ ,  $R_{\text{surfD}}$ , and  $R_{\text{surf}}$ ) dictate the lithium migration path taken during the phase transformation.

Figs. 1 and 4). While larger than technologically relevant battery particles, this particle morphology has been extensively used in fundamental studies<sup>21–23</sup>, and is thin enough to minimize the effect of blocked conduction channels<sup>25</sup>. We estimate the anti-site defect concentration to be between 0.1–0.5% based on Rietveld refinement (Supplementary Table 1).

Figure 2a shows the evolution of the X-ray diffraction (XRD) patterns as the electrochemically prepared, carbon-coated  $\text{Li}_{0.5}\text{FePO}_4$  electrode relaxes in an inert Ar glovebox (<1 ppm  $\text{O}_2$  and  $\text{H}_2\text{O}$ ) at room temperature (see Methods for sample preparation details). We observe the expected (020) peaks for the Li-rich triphylite (LFP) and Li-poor heterosite (FP) at  $29.8^\circ$  and  $30.9^\circ$ , respectively. Because this electrode was electrochemically lithiated at 2 C, where  $C/N$  is the rate to (de)lithiate in  $N$  h, it exhibits significant solid solution behaviour, with the strongest peak at  $30.1^\circ$  likely to be a metastable phase<sup>17,34</sup>. The (211) peaks are weak due to preferential orientation (Supplementary Fig. 4). As the electrode relaxes over hundreds of hours, the solid solution peaks diminish while the LFP and FP peaks grow, confirming that this electrode slowly phase separates. To quantify the solid solution fraction (SSF), we fit Gaussians to the diffraction patterns (Supplementary Fig. 5 and Supplementary Section 3)<sup>19</sup>. The quantified SSF decreases from 57% to 33% after 500 h in Ar. In  $\text{Li}_{0.5}\text{FePO}_4$  particles without carbon coating (Fig. 2b), the SSF also decreases slowly, from 39% to 26% in 100 h. Both electrodes retain significant solid solution character over long times, reflecting a high  $R_{\text{bulk}}$ .

Next, we examined the effect of solvent exposure on the rate of phase transformation in uncoated particles, electrochemically lithiated at 1 C to  $\text{Li}_{0.5}\text{FePO}_4$ . When the electrode is immersed in a salt-free ethylene carbonate/dimethyl carbonate (EC/DMC) solvent, the SSF decreases from 41% to below 30% in just 8 h, more than one order of magnitude enhancement in the phase separation rate. Ambient atmosphere similarly increases the phase separation rate. Solvent, protons<sup>35</sup>, oxygen and water molecules do not intercalate into the bulk of  $\text{Li}_x\text{FePO}_4$ , in part due to large differences in size from the ionic radii of lithium. XRD and transmission electron microscopy detected no secondary phase formation on the (010) facet from exposure to ambient water vapour (Supplementary Fig. 7). This is consistent with the stability of  $\text{Li}_x\text{FePO}_4$  with regard to both oxygen and hydrogen evolution, and its use in aqueous Li-ion batteries<sup>36</sup>. Although we cannot fully rule out chemical reactions between water vapour and the  $\text{Li}_x\text{FePO}_4$  surface, which occur for extended exposure to liquid water<sup>37</sup>, the dominant effect of water vapour here is to facilitate phase separation of the underlying solid solution  $\text{Li}_x\text{FePO}_4$ . Because the phase separation rate is proportional to the lithium migration rate<sup>38</sup>, we propose that solvent and water molecules interact with the lithium on the surface of the particles and activate surface diffusion.

We repeated this experiment for carbon-coated particles, lithiated at 2 C (Fig. 2c). Exposing  $\text{Li}_{0.5}\text{FePO}_4$  to water vapour or to ambient air increases the phase separation rate by at least two orders of magnitude: 8 h of exposure to 11 Torr of water vapour in Ar induces significantly more phase separation than 500 h of exposure to pure Ar (Fig. 2c). The salt-free EC/DMC solvent does not accelerate phase separation in the carbon-coated particles, in contrast to the uncoated particles. The role of the carbon coating in light of our experimental results is discussed in Supplementary Section 3 and warrants further work. We later discuss phase separation in the presence of the electrolyte.

We also directly visualized the distribution of lithium within individual carbon-coated particles using scanning transmission X-ray microscopy (STXM, Fig. 2d). The lithium composition  $X$  is computed from the Fe oxidation state maps by fitting a linear combination<sup>21,32</sup> of  $\text{LiFe}^{2+}\text{PO}_4$  and  $\text{Fe}^{3+}\text{PO}_4$  references (Supplementary Fig. 8a) to the acquired absorption spectra at every pixel. The visible Li-rich, solid solution, and Li-poor domains are significantly larger than the pixel size of 50 nm. According to the STXM results, the particles in the electrode stored in inert Ar are mostly solid solution, whereas the ones stored under ambient air are mostly phase-separated. The SSF, defined as the fraction of pixels where  $0.15 < X < 0.85$ , is  $84 \pm 12\%$  in Ar and only  $32 \pm 10\%$  in air. STXM and XRD here provide complementary information: microscopy confirms that the environment directly alters the lithium composition within particles, and that the observed diffraction patterns do not arise only from elastic strain. Likewise, the significant SSF computed from the (020) reflection (Fig. 2a) confirms that mixed valence (yellow) pixels in STXM do not result from a phase boundary parallel to the (010) facet, or from phase-separated domains too small to be captured with our  $\sim 50$  nm pixel size. Supplementary Figure 9 captures relaxation within a single particle and confirms that phase separation results from spinodal decomposition rather than nucleation and growth.

### Atomistic origins of enhanced surface diffusion

Having established that water and solvent molecules enhance the rate of phase separation in  $\text{Li}_{0.5}\text{FePO}_4$  by at least two orders of magnitude, we investigated the atomic-scale mechanism of lithium diffusion at the solid/fluid interface. We performed ab initio molecular dynamics (MD) calculations on  $\text{LiFePO}_4(010)/\text{water}$ ,  $\text{LiFePO}_4(010)/\text{EC}$  and bare  $\text{LiFePO}_4(010)/\text{vacuum}$  interfaces, building on our previous surface simulation work<sup>39</sup>. Figure 3a illustrates the simulation snapshots indicating the migration of a surface  $\text{Li}^+$

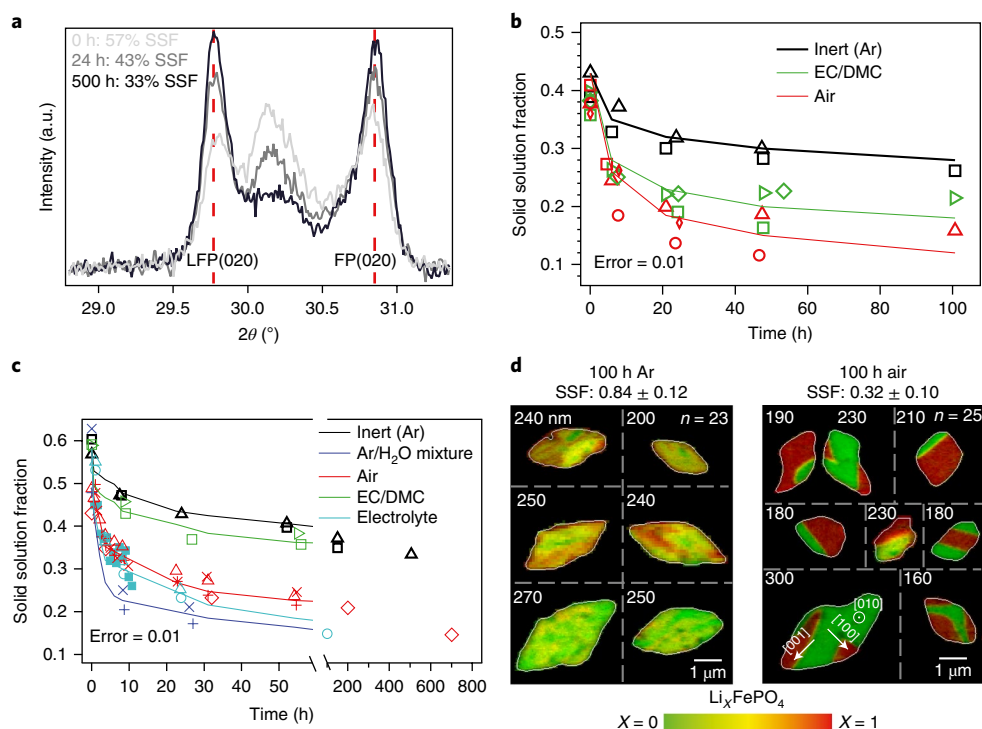


**Fig. 2 | Tracking solid solution  $\text{Li}_{0.5}\text{FePO}_4$  electrodes during phase separation.** **a**, X-ray diffraction of carbon-coated particles as they phase-separate in inert Ar. The (020) peaks for the Li-rich triphylite (LFP) at  $29.8^\circ$  and Li-poor heterosite (FP) at  $30.9^\circ$  grow over time, whereas the aggregate intensity of the intermediate peaks, quantified by the solid solution fraction (SSF), diminish.  $t=0$  corresponds to the XRD patterns ~10 min after the current is interrupted. **b**, The phase separation rate for bare, uncoated particles is heavily increased in solvent and ambient environments. The error of 0.01 equals the difference in the quantified SSF on consecutive scans of the same sample. **c**, Phase separation for carbon-coated particles is also strongly affected by the environment. The filled squares represent in situ diffraction of an electrode relaxing in the battery electrolyte in Fig. 4a. Each marker colour and shape combination in **b** and **c** represents a different electrode; lines are to guide the eye. **d**, Direct STXM imaging of the lithium distribution via Fe oxidation state maps confirms that air significantly enhances the rate of phase separation compared with Ar. The [001] direction is the projected major axis of each platelet; the [100] direction is the minor axis; the [010] direction is the thickness of the platelet and perpendicular to the plane of the page. The thickness in the [010] direction is labelled next to each particle.  $n$  equals the number of imaged particles, and the STXM SSF confidence interval equals two standard errors.

at the  $\text{LiFePO}_4(010)/\text{EC}$  interface. The migrating lithium is located initially at a surface site at the top of a [010] channel. As the simulation proceeds, the  $\text{Li}^+$  coordinates to two EC molecules and a lattice oxygen. The EC molecules lift the  $\text{Li}^+$  from its original position, and then move the  $\text{Li}^+$  to a surface site at the top of a neighbouring [010] channel about  $4.6 \text{ \AA}$  away. Interestingly, the EC molecules are involved in the migration process rather than acting as simple adsorbates, and do not intercalate into the bulk of the material. Other migration pathways are also possible, and the virtue of our MD approach is that such information on molecular and lithium-ion dynamics would not be extracted from purely static simulations based on nudged elastic band methodology. In any case, our ab initio results clearly indicate that the EC molecules facilitate the surface migration of  $\text{Li}^+$ . While not directly simulated, it has been shown that electrons migrate via polaron hopping in the bulk<sup>26</sup>.

MD calculations were also performed for a  $\text{LiFePO}_4(010)/\text{water}$  interface. In a similar fashion to the  $\text{LiFePO}_4(010)/\text{EC}$  interface, water molecules were found to coordinate to  $\text{Li}^+$ , assisting its migration across the surface, illustrated as simulation snapshots in Fig. 3b. In contrast, migration of  $\text{Li}^+$  is not found on the  $\text{LiFePO}_4(010)/\text{vacuum}$  interface during the simulation timescale, which is consistent with the high lithium migration energy ( $\sim 0.9 \text{ eV}$ ) that we calculate on the bare inert (010) surface and agrees with a migration barrier previously reported<sup>29</sup>. Moreover, this result is consistent with the extremely slow rate of phase separation when the particles are stored in Ar gas (Fig. 2). The surface structure considered for these simulations may be modified with coatings and

other phosphate phases<sup>40,41</sup>, which warrants further investigation. In general, the ab initio MD simulation results indicate that the fluid molecules significantly enhance the surface diffusivity, and that this solvent-mediated mechanism is the dominant pathway for in-plane lithium-ion migration.

### Phase transformation in ionically connected particles

Next, we investigated phase transformation in ionically connected, carbon-coated particles by relaxing solid solution particles towards equilibrium in a liquid battery electrolyte (1 M  $\text{LiClO}_4$  in EC/DMC). Here, all lithium redistribution pathways are available (Fig. 1b). In situ and ex situ X-ray diffraction confirm that the particles phase-separate at a rate much faster in the presence of the liquid electrolyte than in inert Ar (Figs. 2c and 4a). Significant phase separation is observed within 2 h of relaxation.

If surface diffusion is faster than the insertion reaction ( $R_{\text{surfD}} < R_{\text{rxn}}$ , Fig. 4b), then lithium is confined to its original particle. Consequently, each solid solution particle initially separates into Li-rich and Li-poor domains<sup>14</sup>, conserving the amount of lithium in each particle. On the other hand, if surface diffusion is slower than the insertion reaction ( $R_{\text{surfD}} > R_{\text{rxn}}$ ) and lithium redistribution occurs via the electrolyte (Fig. 4c), then lithium is also free to move to nearby particles under fast electrolyte transport<sup>31</sup>. Here, the particles directly relax into the globally lowest energy configuration, a mosaic of Li-rich and Li-poor particles that minimizes interfacial<sup>15,42</sup> and strain<sup>14,43</sup> energies associated with intraparticle phase separation. This mosaic pattern, also known as interparticle phase



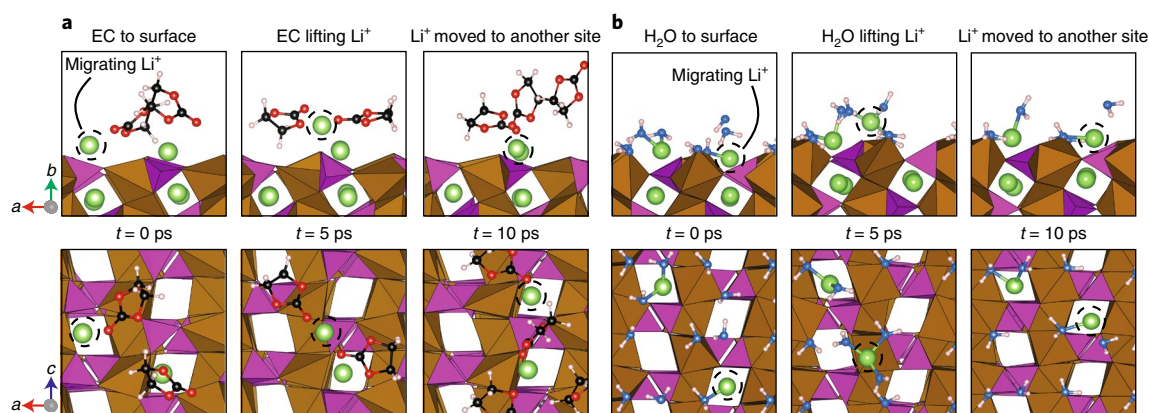


**Fig. 3 | Atomic geometries at the  $\text{LiFePO}_4$  (010)/EC and  $\text{LiFePO}_4$  (010)/ $\text{H}_2\text{O}$  interfaces from ab initio MD simulations indicating Li-ion migration at the surface. **a**,  $\text{LiFePO}_4$  (010)/EC interface. **b**,  $\text{LiFePO}_4$  (010)/ $\text{H}_2\text{O}$  interface. Top and bottom panels show views from the side and above, respectively, at three simulation snapshots with the migrating  $\text{Li}^+$  circled by a dashed line. In the views from above, only the outermost surface  $\text{Li}^+$  ions are shown for clarity. We note that the (010) surface structure is intrinsically Li-deficient relative to the bulk lattice, containing 50% vacant Li sites in the surface layer<sup>39</sup>. Key: Li ions (green); O ions in  $\text{LiFePO}_4$  and EC (red); O in water (blue); H in water and EC (white); C in EC (black);  $\text{PO}_4$  (purple);  $\text{FeO}_6$  (brown).**

separation, arises during (dis)charge at low rates<sup>13,44</sup>. While the electrode will always eventually relax into the lowest-energy mosaic (Fig. 4b,c), an initial observation of intraparticle phase separation would demonstrate that surface diffusion is the dominant pathway for lithium redistribution.

To test this hypothesis, we used STXM to image the lithium distribution within particles. We define actively relaxing particles as the particles where  $0.15 < \bar{X} < 0.85$ ; here,  $\bar{X}$  is the average lithium composition within a particle. Figure 4d–f shows the lithium distribution in particles from  $\text{Li}_{0.5}\text{FePO}_4$  electrodes lithiated at 2C and relaxed under different conditions. In the control experiment (Fig. 4d), the electrode is stored in inert Ar, and the particles remain as solid solutions (SSF  $75 \pm 8\%$ ). The active particle fraction here is  $81 \pm 14\%$  (Fig. 4d). Figure 4e shows a different part of the same electrode that is relaxed for ~8 h in the electrolyte. The active particle fraction decreases slightly to  $71 \pm 16\%$ , but the SSF decreases significantly to  $41 \pm 8\%$ . This result demonstrates that lithium is mostly confined to its original particle during phase separation. After relaxing for 500 h in electrolyte, the active particle fraction decreases to  $38 \pm 20\%$  (Fig. 4f).

The observation that individual particles initially separate into Li-rich and Li-poor domains confirms that lithium is mostly confined to its original particle in the first few hours. Phase-field simulations of two relaxing solid solution particles (Supplementary Fig. 10, described in detail in the next section) verify that this sequence is only observed when surface diffusion is faster than interfacial reaction. The fast surface diffusion during relaxation is a result of lithium not having to cross the double layer or undergoing charge transfer, and is consistent with our results for uncoated  $\text{Li}_{0.5}\text{FePO}_4$  in EC/DMC (Fig. 2b) and our MD simulations (Fig. 3a).

Finally, we show evidence of phase separation in the current–voltage response of the battery cell. We probed the electrochemical resistance of a solid solution electrode as it relaxed at open-circuit (see Supplementary Section 5b for details). Our results clearly show that the resistance of  $\text{Li}_{0.5}\text{FePO}_4$  increases over time across a variety of conditions (Supplementary Fig. 11), doubling over the course of 50 h. In contrast, a solid solution  $\text{Li}_{0.7}(\text{Ni}_{1/3}\text{Co}_{1/3}\text{Mn}_{1/3})\text{O}_2$  electrode exhibits negligible change in the resistance over time (Supplementary Fig. 11b). Phase separation increases the electrochemical resistance due to concentration of current in a smaller number of active particles<sup>32</sup>, decreased active area for intercalation area, and/or lower exchange current density for the phase-separated lithium compositions<sup>21</sup>. The tens of hours

required to increase the electrochemical resistance is consistent with the long times required for intraparticle and/or interparticle phase separation (Fig. 4).

### Phase-field simulations of surface diffusion

We used continuum modelling to explore the effect of surface diffusion on the phase separation behaviour of  $\text{Li}_x\text{FePO}_4$  under constant current conditions. The existing Allen–Cahn reaction model with generalized Butler–Volmer kinetics<sup>30</sup> predicts suppression of phase separation by electro-autocatalysis upon lithium insertion<sup>14,16,21,45</sup>. Here, we unify the Allen–Cahn and Cahn–Hilliard models by adding an in-plane diffusion term to simulate the surface diffusion demonstrated experimentally in the previous sections. The resulting generalized reaction–diffusion equation is given by:

$$\frac{\partial X}{\partial t} = \nabla \left[ \frac{D_{\text{eff}}}{k_B T} X (1-X) \nabla \mu_{\text{Li}} \right] + r(X, \mu_{\text{Li}}, \mu_{\text{ext}}) \quad (1)$$

where  $X$  is the spatially resolved lithium composition,  $t$  the time,  $D_{\text{eff}}$  the average in-plane diffusivity, which is proportional to the surface diffusivity  $D_{\text{surface}}$ ,  $\mu_{\text{Li}}$  the local chemical potential of lithium in  $\text{Li}_x\text{FePO}_4$ ,  $\mu_{\text{ext}} = \mu_{\text{Li}^+} + \mu_{\text{e}^-}$  the external lithium chemical potential established by the electrons in the current collector and the lithium ions in the electrolyte,  $k_B$  the Boltzmann constant, and  $T$  the temperature. These terms control the local rate of lithium insertion  $r$ , which is proportional to the current density  $j$ , and governed by generalized Butler–Volmer kinetics<sup>30</sup> described in Supplementary equation (4) and Supplementary Section 6.

We analysed the linear stability of equation (1) using the formalism derived by Bazant<sup>45</sup>, which determines whether a small perturbation in the lithium composition from a homogeneous solid solution  $X=0.5$  will grow (unstable) or decay (stable) (see Supplementary equations (5) and (6), and Supplementary Fig. 12 for definitions). Linear instability is a necessary but insufficient prerequisite for phase separation. The neutral stability threshold  $j_c$  depends on the current density, the surface diffusivity  $D_{\text{surface}}$  and the exchange current density  $j_0$  (Fig. 5a). As  $D_{\text{surface}} \rightarrow 0$ , the neutral stability threshold is proportional to  $j_0$  and results from the auto-inhibitory form of the composition-dependent  $j_0$  (refs 14,16,21,45). We denote this as regime I. Increasing  $D_{\text{surface}}$  transitions into regime II, where the neutral stability threshold is proportional to  $D_{\text{surface}}$ .

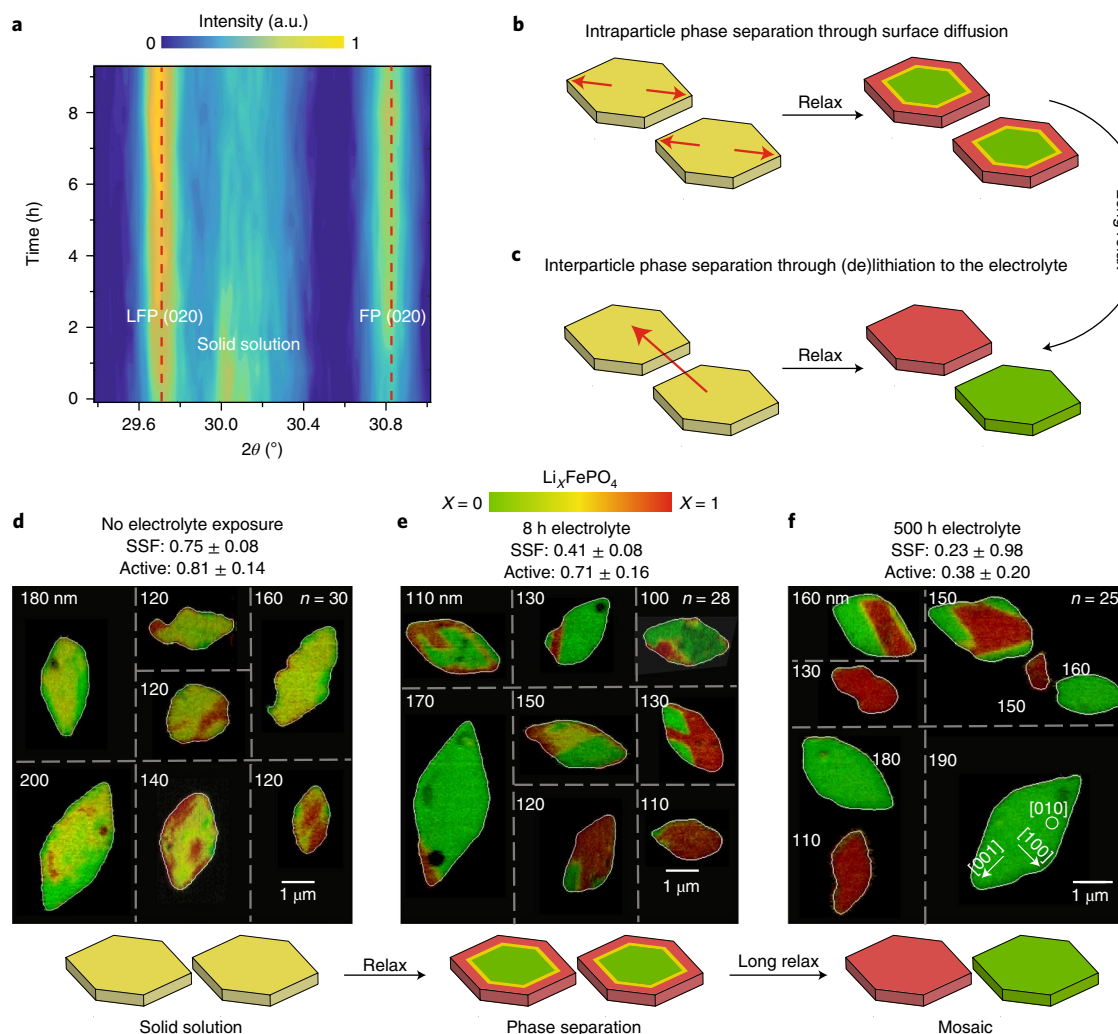


**Fig. 4 | The distribution of lithium in ionically connected particles shows that phase separation occurs primarily via surface diffusion.** **a**, In situ XRD patterns show that solid solution particles separate into Li-rich and Li-poor phases during relaxation; SSF quantification is shown in Fig. 2c. **b,c**, Schematic illustrations of intraparticle and interparticle phase separation. **d–f**, STXM images of the lithium composition distribution under different electrolyte exposure times show solid solution under no electrolyte exposure (**d**), intraparticle phase separation after short, 8-h electrolyte exposure (**e**) and interparticle mosaic under long electrolyte exposure (**f**). The active particle fraction is the fraction of particles with an average composition  $\bar{X}$  between 0.15 and 0.85. The confidence interval represents two standard deviation under a binomial distribution for the active particle fraction or two standard error in terms of the SSF. The particles have the same crystal orientations as in Fig. 2d, and the thickness in the [010] direction is labelled next to each particle. An unpaired *t* test of the active particle fraction between **e** and **f** yields  $t = 2.6$  and a *p* value of 0.01.

To determine if the perturbations grow fast enough to induce phase separation, we simulated a particle lithiating at constant current as a function of the applied current density  $j_{\text{particle}}$  and  $D_{\text{surface}}$  using equation (1). Figure 5b plots the final computed SSF, defined as the fraction of the simulated particle where  $0.15 < X < 0.85$  when  $\bar{X} = 0.5$ . In regime I on the left side of the plot, we observe three regions: linearly stable solid solution (blue), linearly unstable ‘quasi’ solid solution (blue) and phase separation (black), consistent with previous work<sup>14,16</sup>. Supplementary Figure 12 illustrates the differences between the three regions. The threshold current density  $j_s$  approximately defines the boundary between the quasi-solid solution and phase separation behaviour.

As we increase  $D_{\text{surface}}$  in regime II, the threshold  $j_s$  becomes proportional to  $D_{\text{surface}}$ . When  $j < j_s$ , surface diffusion redistributes lithium from a solid solution into Li-rich and Li-poor domains by transporting lithium to the moving phase boundary (Fig. 5c). On the other hand, when  $j > j_s$ , there is not enough time for surface diffusion to redistribute the lithium, creating

(quasi) solid solution particles. Here, lithium incorporates into the particle near its original desolvation site (Fig. 5d). In both cases, the entire (010) surface participates in the reaction. Based on experimental observations of phase separation at a particle rate above 0.1 C (Supplementary Fig. 13), our simulations suggest that  $D_{\text{surface}}$  is at least  $10^{-12} \text{ cm}^2 \text{ s}^{-1}$ , significantly higher than the  $10^{-15} \text{ cm}^2 \text{ s}^{-1}$  calculated for a bare  $\text{FePO}_4$ /vacuum interface<sup>29</sup>. This quasi solid solution appears even when the shape of  $j_0(X)$  does not yield complete suppression of phase separation by electro-autocatalysis (Supplementary Fig. 14).

Our simulations show that decreasing  $D_{\text{surface}}$  slows phase separation driven by electro-autocatalysis to give quasi-solid solutions in regime II. When surface diffusion is too slow to redistribute the lithium (Fig. 5d), the particle behaviour will be governed by reaction kinetics; as a result, electro-autocatalysis with asymmetric  $j_0(X)$  with respect to  $X = 0.5$  results in a broken symmetry in the growth rate of non-uniform domains between lithium insertion and extraction<sup>45</sup>, as observed in previous experiments<sup>21</sup>.

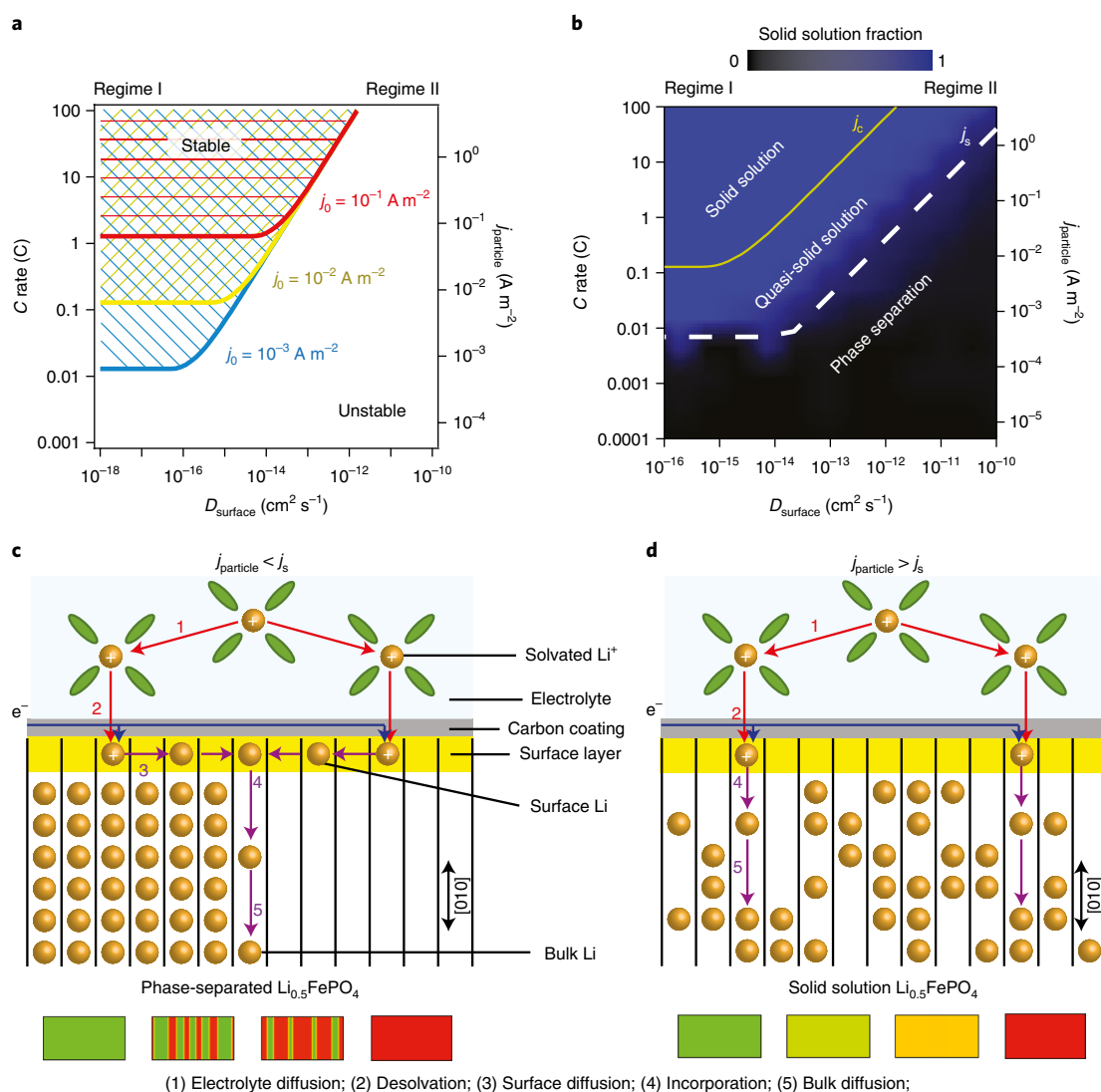


**Fig. 5 | Origin of phase separation and solid solution from single-particle simulations.** **a**, The analytical linear stability condition as functions of the exchange current density and surface diffusivity. The calculations were conducted at  $\bar{X} = 0.5$ . Instability in regime I is driven by reaction, whereas instability in regime II is driven by surface diffusion. **b**, The simulated solid solution fraction (SSF) at  $\bar{X} = 0.5$ .  $j_s$  is defined as the SSF = 0.5 contour and separates solid solution from phase separation.  $j_c$  plots the linear stability curve from **a**. The exchange current density used was  $0.005 \text{ A m}^{-2}$ , previously measured<sup>21</sup>. **c**, During phase separation where  $j_{\text{particle}} < j_s$  in regime II, lithium desolvates on the entire surface, but lithium migrates on the surface before incorporating into the bulk at the phase boundary. **d**, During solid solution where  $j_{\text{particle}} > j_s$ , lithium must be incorporated into the particle near the original desolvation and charge transfer site. Simulated results of phase separation and solid solution in 300 nm particles are shown below the schematics, where the colours have the same meaning as in Fig. 4.

Supplementary Section 7 and Supplementary Fig. 16 extend this discussion to a many-particle electrode. The kinetic ‘phase diagrams’ in Fig. 5 and Supplementary Fig. 16 establish how electro-autocatalytic reaction kinetics, C-rate and surface diffusivity conspire to control the phase transformation pathway for  $\text{Li}_x\text{FePO}_4$ , in both single and many particles. Our simulation suggests that surface diffusion should be minimized to obtain (quasi) solid solutions within individual particles (Fig. 5b and Supplementary Fig. 16c), and that C-rate should be high relative to the exchange current density to obtain concurrent, non-mosaic intercalation in the porous electrode (Supplementary Fig. 16).

Our demonstration of fluid-enhanced surface diffusion in electrochemically active materials introduces new paradigms for controlling phase transformations in anisotropic mixed ionic and electronic conductors, where transport could be dominated by surface diffusion. We show that engineering the solid/fluid

interface controls the bulk phase transformation behaviour. Moreover, because solid solution particles have lower interfacial resistances (Supplementary Fig. 11), suppressing surface diffusion and phase separation may yield higher roundtrip energy efficiencies. Minimizing surface diffusion without altering the bulk solid could be achieved by either modifying the fluid (for example, introducing small amounts of electrolyte additives) or by coating the surface. Surface diffusion may also be suppressed altogether in solid-state batteries without electrolyte solvents. We recognize, however, that phase separation is an intrinsic thermodynamic property of the material, and that even dramatically decreased surface diffusion will not completely suppress phase separation because of the parallel electrolyte and bulk diffusion pathways (Fig. 1b). We also note that lowering surface diffusivity may simultaneously create undesirable effects such as reduced reaction rate.



In a broader context, the ability to suppress phase separation by minimizing surface diffusion is crucial towards lowering coherence strain, reducing mechanical fracture and creating longer-lasting devices<sup>46</sup>. Such insights may be especially relevant for high-volume-expansion electrodes such as silicon. Beyond batteries, the control of phase transformation through surface diffusion is also applicable to anisotropic geometries such as thin films, layered materials, nanowires, and highly porous structures where the bulk diffusion rates vary significantly in different directions. For example, moisture-activated surface diffusion tunes memristive switching in thin films<sup>4</sup>. Surface diffusion can control phase transformations in alloying silicon nanowires<sup>47</sup>, with one possible pathway schematically shown in Supplementary Fig. 17. Layered materials including graphite, transition metal dichalcogenides, and MXenes often exhibit anisotropic diffusivities and phase separation on ion insertion<sup>48,49</sup>; if bulk diffusivities between or within layers are slow, surface diffusion may provide important contributions towards phase transformation kinetics. Our generalized reaction–diffusion model can quantitatively simulate this behaviour across diverse materials systems. Finally, by activating transport at the solid/liquid interface, nominally insulating materials may now be used as solid electrodes, electrolytes and electrocatalysts, such as the surface diffusion of lithium polysulfide species in the Li–S battery<sup>50</sup>.

In summary, we have demonstrated that surface diffusion of lithium ions facilitated by solvent molecules makes  $\text{Li}_x\text{FePO}_4$  a ‘three-dimensional’ conductor. This surface diffusion is a missing link that controls the phase transformation rate in  $\text{Li}_x\text{FePO}_4$  and determines the current threshold between phase separation and solid solution. This current threshold is well within the range of operation for typical Li-ion batteries, such as the time-averaged discharge of portable electronic devices over one day. We show that the balance between insertion kinetics, cycling rate and the surface ion diffusivity governs the phase behaviour of  $\text{Li}_x\text{FePO}_4$ . By establishing that select molecules can be used to tune the surface diffusion rate, our work demonstrates a facile method to control phase separation, which is especially relevant for anisotropic and nanosized materials. We show that surface diffusion must also be considered for both mechanistic understanding and improved device performance. More broadly, we provide a general framework for phase transformation mechanisms in anisotropic materials where the phase boundary movement and ion flux directions are orthogonal.

## Online content

Any methods, additional references, Nature Research reporting summaries, source data, statements of data availability and associated accession codes are available at <https://doi.org/10.1038/s41563-018-0168-4>.

Received: 3 April 2017; Accepted: 14 August 2018;

Published online: 17 September 2018

## References

- Grey, C. P. & Tarascon, J. M. Sustainability and in situ monitoring in battery development. *Nat. Mater.* **16**, 45–56 (2017).
- Griessen, R., Strohheldt, N. & Giessen, H. Thermodynamics of the hybrid interaction of hydrogen with palladium nanoparticles. *Nat. Mater.* **15**, 311–317 (2016).
- Trotochaud, L., Ranney, J. K., Williams, K. N. & Boettcher, S. W. Solution-cast metal oxide thin film electrocatalysts for oxygen evolution. *J. Am. Chem. Soc.* **134**, 17253–17261 (2012).
- Messerschmitt, F., Kubicek, M. & Rupp, J. L. M. How does moisture affect the physical property of memristance for anionic-electronic resistive switching memories? *Adv. Funct. Mater.* **25**, 5117–5125 (2015).
- Padhi, A. K., Nanjundaswamy, K. S. & Goodenough, J. B. Phospho-olivines as positive-electrode materials for rechargeable lithium batteries. *J. Electrochem. Soc.* **144**, 1188–1194 (1997).
- Delacourt, C., Poizot, P., Tarascon, J.-M. & Masquelier, C. The existence of a temperature-driven solid solution in  $\text{Li}_x\text{FePO}_4$  for  $0 \leq x \leq 1$ . *Nat. Mater.* **4**, 254–260 (2005).
- Yamada, A. et al. Room-temperature miscibility gap in  $\text{Li}_x\text{FePO}_4$ . *Nat. Mater.* **5**, 357–360 (2006).
- Tang, M., Carter, W. C. & Chiang, Y.-M. Electrochemically driven phase transitions in insertion electrodes for lithium-ion batteries: examples in lithium metal phosphate olivines. *Annu. Rev. Mater. Res.* **40**, 501–529 (2010).
- Gibot, P. et al. Room-temperature single-phase Li insertion/extraction in nanoscale  $\text{Li}_x\text{FePO}_4$ . *Nat. Mater.* **7**, 741–747 (2008).
- Morgan, D., Van der Ven, A. & Ceder, G. Li conductivity in  $\text{Li}_x\text{MPO}_4$  (M = Mn, Fe, Co, Ni) olivine materials. *Electrochem. Solid State Lett.* **7**, A30–A32 (2004).
- Islam, M. S., Driscoll, D. J., Fisher, C. A. J. & Slater, P. R. Atomic-scale investigation of defects, dopants, and lithium transport in the  $\text{LiFePO}_4$  olivine-type battery material. *Chem. Mater.* **17**, 5085–5092 (2005).
- Delmas, C., Maccario, M., Croguennec, L., Le Cras, F. & Weill, F. Lithium deintercalation in  $\text{LiFePO}_4$  nanoparticles via a domino-cascade model. *Nat. Mater.* **7**, 665–671 (2008).
- Dreyer, W. et al. The thermodynamic origin of hysteresis in insertion batteries. *Nat. Mater.* **9**, 448–453 (2010).
- Cogswell, D. A. & Bazant, M. Z. Coherency strain and the kinetics of phase separation in  $\text{LiFePO}_4$  nanoparticles. *ACS Nano* **6**, 2215–2225 (2012).
- Malik, R., Zhou, F. & Ceder, G. Kinetics of non-equilibrium lithium incorporation in  $\text{LiFePO}_4$ . *Nat. Mater.* **10**, 587–590 (2011).
- Bai, P., Cogswell, D. A. & Bazant, M. Z. Suppression of phase separation in  $\text{LiFePO}_4$  nanoparticles during battery discharge. *Nano Lett.* **11**, 4890–4896 (2011).
- Orikasa, Y. et al. Direct observation of a metastable crystal phase of  $\text{Li}_x\text{FePO}_4$  under electrochemical phase transition. *J. Am. Chem. Soc.* **135**, 5497–5500 (2013).
- Zhang, X. et al. Rate-induced solubility and suppression of the first-order phase transition in olivine  $\text{LiFePO}_4$ . *Nano Lett.* **14**, 2279–2285 (2014).
- Liu, H. et al. Capturing metastable structures during high-rate cycling of  $\text{LiFePO}_4$  nanoparticle electrodes. *Science* **344**, 1252817 (2014).
- Zhang, X. et al. Direct view on the phase evolution in individual  $\text{LiFePO}_4$  nanoparticles during Li-ion battery cycling. *Nat. Commun.* **6**, 8333 (2015).
- Lim, J. et al. Origin and hysteresis of lithium compositional spatiodynamics within battery primary particles. *Science* **353**, 566–571 (2016).
- Chen, G., Song, X. & Richardson, T. J. Electron microscopy study of the  $\text{LiFePO}_4$  to  $\text{FePO}_4$  phase transition. *Electrochem. Solid State Lett.* **9**, A295–A298 (2006).
- Yu, Y.-S. et al. Dependence on crystal size of the nanoscale chemical phase distribution and fracture in  $\text{Li}_x\text{FePO}_4$ . *Nano Lett.* **15**, 4282–4288 (2015).
- Nishimura, S. et al. Experimental visualization of lithium diffusion in  $\text{Li}_x\text{FePO}_4$ . *Nat. Mater.* **7**, 707–711 (2008).
- Malik, R., Burch, D., Bazant, M. & Ceder, G. Particle size dependence of the ionic diffusivity. *Nano Lett.* **10**, 4123–4127 (2010).
- Amin, R., Maier, J., Balaya, P., Chen, D. P. & Lin, C. T. Ionic and electronic transport in single crystalline  $\text{LiFePO}_4$  grown by optical floating zone technique. *Solid State Ionics* **179**, 1683–1687 (2008).
- Tealdi, C., Spreafico, C. & Mustarelli, P. Lithium diffusion in  $\text{Li}_{1-x}\text{FePO}_4$ : the effect of cationic disorder. *J. Mater. Chem.* **22**, 24870–24876 (2012).
- Hong, L. et al. Two-dimensional lithium diffusion behavior and probable hybrid phase transformation kinetics in olivine lithium iron phosphate. *Nat. Commun.* **8**, 114 (2017).
- Dathar, G. K. P., Sheppard, D., Stevenson, K. J. & Henkelman, G. Calculations of Li-ion diffusion in olivine phosphates. *Chem. Mater.* **23**, 4032–4037 (2011).
- Bazant, M. Z. Theory of chemical kinetics and charge transfer based on nonequilibrium thermodynamics. *Acc. Chem. Res.* **46**, 1144–1160 (2013).
- Marom, R., Haik, O., Aurbach, D. & Halalay, I. C. Revisiting  $\text{LiClO}_4$  as an electrolyte for rechargeable lithium-ion batteries. *J. Electrochem. Soc.* **157**, A972 (2010).
- Li, Y. et al. Current-induced transition from particle-by-particle to concurrent intercalation in phase-separating battery electrodes. *Nat. Mater.* **13**, 1149–1156 (2014).
- Ferguson, T. R. & Bazant, M. Z. Nonequilibrium thermodynamics of porous electrodes. *J. Electrochem. Soc.* **159**, A1967–A1985 (2012).
- Koyama, Y. et al. Hidden two-step phase transition and competing reaction pathways in  $\text{LiFePO}_4$ . *Chem. Mater.* **29**, 2855–2863 (2017).
- Benedek, R., Thackeray, M. M. & Van De Walle, A. Free energy for protonation reaction in lithium-ion battery cathode materials. *Chem. Mater.* **20**, 5485–5490 (2008).
- Luo, J.-Y., Cui, W.-J., He, P. & Xia, Y.-Y. Raising the cycling stability of aqueous lithium-ion batteries by eliminating oxygen in the electrolyte. *Nat. Chem.* **2**, 760–765 (2010).
- Zaghib, K. et al. Aging of  $\text{LiFePO}_4$  upon exposure to  $\text{H}_2\text{O}$ . *J. Power Sources* **185**, 698–710 (2008).
- Cahn, J. W. On spinodal decomposition. *Acta Metall.* **9**, 795–801 (1961).
- Fisher, C. A. J. & Islam, M. S. Surface structures and crystal morphologies of  $\text{LiFePO}_4$ : relevance to electrochemical behaviour. *J. Mater. Chem.* **18**, 1209–1215 (2008).

40. Zaghib, K., Mauger, A., Gendron, F. & Julien, C. M. Surface effects on the physical and electrochemical properties of thin  $\text{LiFePO}_4$  particles. *Chem. Mater.* **20**, 462–469 (2008).
41. Rho, Y., Nazar, L. F., Perry, L. & Ryan, D. Surface chemistry of  $\text{LiFePO}_4$  studied by Mössbauer and X-ray photoelectron spectroscopy and its effect on electrochemical properties. *J. Electrochem. Soc.* **154**, A283–A289 (2007).
42. Wagemaker, M., Mulder, F. M. & Van Der Ven, A. The role of surface and interface energy on phase stability of nanosized insertion compounds. *Adv. Mater.* **21**, 2703–2709 (2009).
43. Cogswell, D. A. & Bazant, M. Z. Theory of coherent nucleation in phase-separating nanoparticles. *Nano Lett.* **13**, 3036–3041 (2013).
44. Ferguson, T. R. & Bazant, M. Z. Phase transformation dynamics in porous battery electrodes. *Electrochim. Acta* **146**, 89–97 (2014).
45. Bazant, M. Z. Thermodynamic stability of driven open systems and control of phase separation by electroautocatalysis. *Faraday Discuss.* **199**, 423–463 (2017).
46. Woodford, W. H., Carter, W. C. & Chiang, Y.-M. Design criteria for electrochemical shock resistant battery electrodes. *Energy Environ. Sci.* **5**, 8014–8024 (2012).
47. Katsman, A., Beregovsky, M. & Yaish, Y. E. Formation and evolution of nickel silicide in silicon nanowires. *IEEE Trans. Electron Devices* **61**, 3363–3371 (2014).
48. Wang, H., Yuan, H., Hong, S. S., Li, Y. & Cui, Y. Physical and chemical tuning of two-dimensional transition metal dichalcogenides. *Chem. Soc. Rev.* **44**, 2664–2680 (2014).
49. Anasori, B., Lukatskaya, M. & Gogotsi, Y. 2D metal carbides and nitrides (MXenes) for energy storage. *Nat. Rev. Mater.* **2**, 16098 (2017).
50. Tao, X. et al. Balancing surface adsorption and diffusion of lithium-polysulfides on nonconductive oxides for lithium-sulfur battery design. *Nat. Commun.* **7**, 11203 (2016).

## Acknowledgements

This experimental work at Stanford and SLAC was supported by the US Department of Energy (DOE), Office of Basic Energy Sciences, Division of Materials Sciences and Engineering under contract DE-AC02-76SF00515. Phase-field theoretical work at MIT and Stanford was supported by the Toyota Research Institute through D3BATT: Center for Data-Driven Design of Li-Ion Batteries. The Advanced Light Source and the Stanford Synchrotron Radiation Lightsource are supported by the DOE Office of Basic

Energy Sciences under contracts DE-AC02-05CH11231 and DE-AC02-76SF00515. M.S.I. and H.C. acknowledge support from the EPSRC (grant EP/K016288) and the Archer HPC facilities through the Materials Chemistry Consortium (EP/L000202). Y.L. and P.M.A. were supported by the NSF Graduate Research Fellowship under grant DGE-114747. K.L. was supported by the Kwanjeong Education Foundation Fellowship. M.Z.B. was supported by the Global Climate and Energy Project at Stanford University and the DOE Office of Basic Energy Sciences through the SUNCAT Center for Interface Science and Catalysis. Part of this work was conducted at the Stanford Nano Shared Facilities. We thank W. D. Nix (Stanford) for insightful discussions on metallurgy and mechanical properties and R. B. Smith (MIT) for assistance with the phase-field model. We also thank A. L. D. Kilcoyne (Berkeley) and D. Shaprio (Berkeley) for assistance with synchrotron measurements.

## Author contributions

Y.L. conceived and designed the project, analysed the experimental data and performed the phase-field simulations. H.C. and M.S.I. conducted the molecular dynamics simulations. Y.L., K.L. and J.H. conducted diffraction. Y.L., J.L., P.M.A., N.J., W.E.G. and Y.S.Y. collected the X-ray microscopy images. S.C.L. performed transmission electron microscopy. D.F., Y.L. and M.Z.B. designed and executed the linear stability analysis. H.D.D., J.M. and M.G. quantified the resistance increase during relaxation. M.S.I. supervised the molecular dynamics simulations. M.Z.B. supervised the phase-field simulations and linear stability analysis. W.C.C. supervised the experimental components of the work. All authors contributed to writing the text.

## Competing interests

The authors declare no competing interests.

## Additional information

**Supplementary information** is available for this paper at <https://doi.org/10.1038/s41563-018-0168-4>.

**Reprints and permissions information** is available at [www.nature.com/reprints](http://www.nature.com/reprints).

**Correspondence and requests for materials** should be addressed to M.S.I. or M.Z.B. or W.C.C.

**Publisher's note:** Springer Nature remains neutral with regard to jurisdictional claims in published maps and institutional affiliations.



## Methods

**Synthesis of  $\text{LiFePO}_4$  particles.**  $\text{LiFePO}_4$  microplatelets were solvothermally synthesized using a mixed water and polyethylene glycol solvent based on our previous work<sup>21</sup>. All precursors for solvothermal synthesis were purchased from Sigma-Aldrich. 6 ml of 1 M  $\text{H}_3\text{PO}_4(\text{aq})$  was mixed with 24 ml of polyethylene glycol 400. Afterwards, 18 ml of 1 M  $\text{LiOH}(\text{aq})$  was added to create the creamy-white  $\text{Li}_3\text{PO}_4$  precipitate. This mixture was bubbled with dry  $\text{N}_2$  for ~16 h in a Schlenk line to remove dissolved oxygen. 6 mmol of  $\text{FeSO}_4 \cdot 7\text{H}_2\text{O}$  was dried under vacuum in a Schlenk line for ~16 h. Next, we transferred 12 ml of deoxygenated  $\text{H}_2\text{O}$  to dissolve the dried  $\text{FeSO}_4$  powder. The lime-green  $\text{FeSO}_4$  solution was transferred without air exposure to the  $\text{Li}_3\text{PO}_4$  suspension, and the entire mixture was transferred to a 100 ml Teflon-lined autoclave in a glovebag. The autoclave was heated to 140 °C for 1 h, then to 210 °C for 17 h, and cooled. The majority of the particles reported in this manuscript are ~170 nm thick and came from the same synthesis batch. The particles used in Figs. 2d and 4a, and Supplementary Fig. 13 came from a different synthesis batch and are ~250 nm thick due to batch-to-batch variations, and show very similar quantified SSF when relaxed in Ar according to Figs. 2d and 4d.

After the synthesis completed, the white  $\text{LiFePO}_4$  particles were centrifuged three times with deionized water and dried. Carbon-coating was conducted by mixing the  $\text{LiFePO}_4$  with sucrose at a mass ratio of 5:1 ( $\text{LiFePO}_4$ :sucrose) without breaking the primary particles. This sample was heated to 600 °C for 5 h in a tube furnace under flowing Ar to yield the carbon-coated  $\text{LiFePO}_4$ . Bare, uncoated particles were annealed under the same condition without mixing with sucrose.

Next, we assembled the electrodes containing 65 wt%  $\text{LiFePO}_4$  particles (coated or uncoated), 25 wt% C65 carbon black and 10 wt% polyvinylidene fluoride binder (MTI). The suspension was cast onto carbon-coated Al foil using a doctor blade with a nominal thickness of 10  $\mu\text{m}$ , and dried under vacuum at 90 °C for ~12 h. Next, coin cells were assembled in an Ar glove box using a 9-mm-diameter  $\text{LiFePO}_4$  electrode, 2 Celgard separators and a 1.2-mm Li metal counter electrode (Alfa Aesar). The electrolyte was 1 M  $\text{LiClO}_4$  dissolved in a 1:1 (wt/wt) mixture of ethylene carbonate (EC) and dimethyl carbonate (DMC). To measure the capacity, the electrodes were cycled at 15  $\text{mA g}^{-1}$  (Supplementary Fig. 3) between 2 V and 4 V. After holding the electrode voltage at 4 V for 6 h on the completion of constant current cycling, the remaining LFP (020/211) peak is ~8% of the combined LFP and FP (020/211) peaks' intensities, suggesting that 8% of the particles are inactive or disconnected (Supplementary Fig. 6). This explains most of the reduced capacity of our electrodes (150  $\text{mAh g}^{-1}$  obtained versus 170  $\text{mAh g}^{-1}$  theoretical). Using STXM, the quantified lithium composition of the particle used as the  $\text{LiFePO}_4$  and  $\text{FePO}_4$  reference are 0.97 and 0.02, respectively, and are spatially homogeneous (Supplementary Fig. 8).

**Preparation of samples for ex situ XRD and STXM.** To prepare the  $\text{Li}_{0.5}\text{FePO}_4$  electrodes with significant initial solid solution fractions, we electrochemically inserted half a formula unit of lithium into a delithiated  $\text{FePO}_4$  composite electrode at a constant current of 1 C (for uncoated particles) or 2 C (for carbon-coated particles) at room temperature (Supplementary Fig. 3).  $C/N$  describes the current to (de)lithiate the electrode in Nh. The electrolyte is 1.0 M  $\text{LiClO}_4$  dissolved in a 1:1 mixture of EC and DMC. Next, we extracted the electrodes from the battery cells, rinsed them with excess DMC solvent to remove the electrolyte, dried the electrodes under vacuum and stored the electrodes in different environments, including inert Ar, air, salt-free EC/DMC mixture, and electrolyte.

**X-ray diffraction.** Except for the synchrotron powder diffraction used in Supplementary Fig. 2, X-ray powder diffraction was conducted using a Cu K- $\alpha$  source and a one-dimensional detector in a Bragg-Brentano geometry. We used both a Bruker D8 Advance and PANAnalytical X'Pert. Ex situ powder diffraction was conducted on the electrodes after they are extracted from the coin cells and rinsed with excess DMC. Because the diffractometer is not located in an inert glovebox, the electrode was exposed to ambient atmosphere for about 10 min for each ex situ measurement before being placed back into the appropriate environment.

In situ X-ray powder diffraction consisted of a battery half-cell housed in a plastic pouch. The pouch cell design is based on our previous work<sup>21</sup>, but the plastic pouch housing used here contains an ~2  $\mu\text{m}$  aluminium lining to further reduce water and oxygen diffusion through the pouch. The  $\text{Li}_x\text{FePO}_4$  positive

electrode, lithium foil negative electrode, Celgard separator, battery electrolyte, and nickel and aluminium current collector tabs were assembled into the pouch. The electrochemical cycling profile of this pouch cell is identical to that of coin cells.

During cycling, the pouch was clamped between two metal plates. After lithiating the positive electrode at 2 C for 15 min, we removed the pouch cell from the clamp and conducted X-ray diffraction on the electrode sitting in the pouch. This removal process took less than 5 min, and the sealed pouch was not opened at any point during the measurement. X-ray diffraction was conducted in a Bruker D8 in a standard reflection mode geometry using a  $\theta$ - $2\theta$  scan between  $2\theta$  values of 28.5° and 32°. 50 measurements taking ~12 min each were conducted. The solid solution fraction for the in situ measurements in Fig. 4a were quantified identically to those of the ex situ measurements in Fig. 2a–c. The  $\text{Li}_x\text{FePO}_4$  electrode remained inside the electrolyte environment of the cell throughout the in situ measurement, and was not exposed to air at any point.

**Scanning transmission X-ray microscopy.** The extracted electrodes were sonicated in dimethyl carbonate and dispersed onto lacey carbon transmission electron microscopy (TEM) grids, and placed in the X-ray microscope. The sample was stored in a glovebox and sealed in an aluminium-lined plastic pouch for transportation. STXM was conducted at the Advanced Light Source, beam line 5.3.2.2 at the Fe  $L_3$  edge. Supplementary Section 4 and Supplementary Fig. 8 contain more details on the STXM analysis protocol including the thickness determination.

**Ab initio calculations.** Ab initio calculations were based on density functional theory as applied successfully to a range of lithium battery materials<sup>52–54</sup>. Here, the VASP code<sup>55</sup> was used with the PBEsol exchange-correlation functional<sup>56</sup> and an energy cut-off for plane-waves of 400 eV. Interactions between core and valence electrons are described by the projector augmented wave (PAW) method. The gamma-point is used for the Brillouin zone sampling. Molecular dynamics simulations were performed using the NVT ensemble with a Nose-Hoover thermostat. Each interface is simulated at 500 K with a time step of 1.5 fs for 15 ps. The  $\text{LiFePO}_4$  (010)/ $\text{H}_2\text{O}$  interface is modelled by a seven-layer  $\text{LiFePO}_4$  slab along the  $b$  axis and a cross-section of a  $1 \times 2$   $ac$  plane, and 8 water molecules above the surface. The  $\text{LiFePO}_4$  (010)/EC interface is modelled using the same  $\text{LiFePO}_4$  slab configuration and 4 EC molecules above the surface.

**Supplementary methods.** The data analysis and the phase-field modelling protocols are given in the Supplementary Information.

**Code availability.** The code for the phase-field model as well as the ab initio calculations will be made available upon reasonable request to the authors.

## Data availability

All experimental data within the article and its Supplementary Information will be made available upon reasonable request to the authors.

## References

- Nelson Weker, J., Li, Y., Shanmugam, R., Lai, W. & Chueh, W. C. Tracking non-uniform mesoscale transport in  $\text{LiFePO}_4$  agglomerates during electrochemical cycling. *ChemElectroChem* **2**, 1576–1581 (2015).
- Islam, M. S. & Fisher, C. A. J. Lithium and sodium battery cathode materials: computational insights into voltage, diffusion and nanostructural properties. *Chem. Soc. Rev.* **43**, 185–204 (2014).
- Ceder, G. Opportunities and challenges for first-principles materials design and applications to Li battery materials. *MRS Bull.* **35**, 693–702 (2010).
- Meng, Y. S. & Dompablo, M. E. A. Computational research of cathode materials for lithium-ion batteries. *Acc. Chem. Res.* **46**, 1171–1180 (2013).
- Kresse, G. & Furthmu, J. Efficient iterative schemes for ab initio total-energy calculations using a plane-wave basis set. *Phys. Rev. B* **54**, 11169–11186 (1996).
- Perdew, J. P. et al. Restoring the density-gradient expansion for exchange in solids and surfaces. *Phys. Rev. Lett.* **100**, 136406 (2008).